Overlap population diagram for ELNES and XANES: peak assignment and interpretation

Overlap population diagram for ELNES and XANES: peak assignment and interpretation

Teruyasu Mizoguchi

Institute of Engineering Innovation, The University of Tokyo, Yayoi, Bunkyo,
Tokyo 113-8656, Japan

Abstract
This article reviews overlap population (OP) diagrams for electron energy loss near-edge structure (ELNES) and x-ray absorption near-edge structure (XANES). By using the OP diagrams, peaks in ELNES and XANES of MgO, ZnO, AlN, GaN, InN, and $YBa_2Cu_3O_{7-x}$ are interpreted in terms of cation–anion and cation–cation interactions. Common features are found in the OP diagrams for different edges. A reconstruction of the unoccupied electronic structure is demonstrated by aligning the different edges with the common features in the OP diagrams. The OP diagram is also applied to the Cu/Al_2O_3 hetero-interface to find the relationships among ELNES, atomic and electronic structures, and properties.

1. Introduction

Both electron energy loss near-edge structures (ELNES) and x-ray absorption near-edge structures (XANES) arise from an electronic transition from a core orbital to unoccupied bands. Since the electron transition responsible for the ELNES and XANES usually follows a dipole selection rule, the spectral features reflect the partial density of states (PDOS) in the unoccupied bands. Therefore, ELNES and XANES can provide information about atomic and electronic structures around an objective atom [1–3].

ELNES is measured by an electron energy loss spectrometer (EELS) which is equipped with transmission electron microscopy (TEM) or scanning TEM (STEM). Employing modern STEM-EELS systems, an observation of edge structures with sub-eV energy resolution and sub-nanometer spatial resolution is possible [4–6]. Therefore, ELNES has potential to elucidate the atomic and electronic structures in the nano- or Å-region, such as small particles, stacking faults, and interfaces. On the other hand, XANES has great advantage in the lower detectable limit. By combining the third generation synchrotron facilities with high-sensitive detectors, XANES from ultradilute dopants of a few ppm level can be measured with sufficient signal to noise ratio [7, 8]. Since these lattice imperfections, such as small particles, stacking faults, interfaces, and dopants, influence the material properties very much, ELNES and XANES are indispensable tools for modern material characterizations.

On the other hand, interpretations of the observed ELNES and XANES data are not always straightforward. ELNES and XANES have been interpreted by comparing with several experimental spectra of reference compounds, namely the 'experimental fingerprint' method. However, it is not always possible to find appropriate and reasonable reference compounds, and one also needs to keep in mind that the atomic and electronic structures around these lattice imperfections are often different from those of bulk compounds. A theoretical tool is essential to interpret the ELNES and XANES.

Recently, quantitative reproductions of experimental spectra have been reported [9–23]. In such theoretical calculations, the following three conditions were commonly fulfilled. The first one is the introduction of a core-hole effect in the calculation. The core hole is the electronic hole at the core orbital, which is generated in the electronic transition from the core orbital to the unoccupied bands. Recent quantitative calculations revealed that the inclusion of the core-hole effects is mandatory. The second important point is the use of a sufficiently large supercell. From the authors' experience, a supercell composed of approximately 100 atoms is necessary to minimize the interactions among the core holes in adjacent cells. By using such large supercells, an excited atom which has a core hole can be separated from other excited atoms in adjacent cells by more than 1 nm. The last one is the computation of the electric dipole transition probability from the core orbital to the unoccupied bands. Through such steps, quantitative reproduction of experimental spectra is possible.

However, even though the calculations quantitatively reproduce the experimental spectra, relationships between the spectra and physical properties are still ambiguous. One must know that relationships between spectral features and information about atomic and electronic structures are not always direct or proportional, because the conduction band, which is responsible for ELNES and XANES, is not identical to the valence band.

To find connections between the spectral features and the physical properties, 'reproduction' of the experimental spectrum is not enough. Peak assignment, namely beyond the 'reproduction', is required. Although partial densities of states (PDOSs) have been used to interpret the spectrum, the electronic structure of the conduction band is quite complicated and the PDOS cannot give the bonding information directly. Even when one orbital seems to overlap with another orbital in a PDOS diagram, they sometimes do not have direct bonding with each other in real space.

Here, an overlap population (OP) diagram is used for peak assignments of ELNES and XANES. The OP diagram is sometimes called a 'COOP (crystal orbital overlap population) diagram' [24], and a combination of band structure calculations with the OP diagram was recently proposed as a powerful method to interpret the ELNES and XANES [6, 25, 26].

In this review, the OP diagram is systematically applied to the ELNES and XANES of MgO [25], ZnO, AlN, GaN, InN, YBa$_2$Cu$_3$O$_{7-x}$ [6], and the Cu/Al$_2$O$_3$ interface [26].

2. Methodology

2.1. Computational procedure

An orthogonalized linear combination of atomic orbitals (OLCAO) method within the local-density approximation (LDA) of the density-functional theory (DFT) was employed to calculate and interpret ELNES and XANES [27]. In this method, core orbitals can be eliminated from the final secular equation by an orthogonalization process. This step can significantly reduce the computational time, and is effective to calculate ELNES and XANES from large and/or complex systems. In addition, atomic orbitals $u_i(r)$ are expressed by the sum of Gaussian functions, and they are used as basis functions. Thereby, chemical bonding information, such as partial density of states, net charges, and bond overlap populations, can be directly obtained. The one-electron wavefunction is expressed as

$$\phi_n(r) = \sum_{i,\gamma} A_{i,\gamma}(k) \cdot b_{i,\gamma}(k, r) \quad (1)$$

where n labels a band index, $A_{i,\gamma}(k)$ is a coefficient, and

$$b_{i,\gamma}(k, r) = \frac{1}{\sqrt{N}} \sum_{\nu} \exp(ikr) \cdot u_i(r - t_\gamma - R_\nu) \quad (2)$$

is the Bloch function of the ith orbital of the γth atom. t_γ is the position vector of the γth atom in the νth cell. R_ν is the lattice translation vector. In the self-consistent

iteration for a stable electronic structure, a full basis function set was employed. After the iteration, we made separate calculations using minimal basis sets in order to calculate the chemical bondings. On the other hand, since the ELNES and XANES comes from unoccupied bands up to 50 eV higher than the Fermi level energy, an extended basis set was applied in the ELNES and XANES calculation. The sets of the employed wavefunctions have been summarized elsewhere [16, 25, 26, 40].

As described above, the core-hole effect is indispensable for the ELNES and XANES calculation [9–23]. In this study, it was fully taken into account in the self-consistent iterations by removing an electron from the core orbital and putting it into the lowest unoccupied band. In order to introduce the core hole in the OLCAO method, only the core orbital of the excited atom which has a core hole was excluded from the orthogonalized process. The theoretical spectrum was obtained by calculating the electron dipole transition probability (I) from a core orbital to the unoccupied bands as follows:

$$I \propto \sum_f |\langle f| q \cdot r |i\rangle|^2 \delta(\hbar\omega - E_f + E_i) \quad (3)$$

f and i are the one-electron wavefunctions in the final state and the initial (ground) state. $\hbar\omega$, E_f, and E_i are the transition energy and the total energies of the supercell in the final state and the ground state, respectively. r is the position of the electron. q is the momentum transfer vector of the scattered electron. Both the final and the ground states were separately calculated. The theoretical transition energy was evaluated by the subtraction of the total energy of the supercell in the ground state from that in the final state. Each transition probability calculated by the above equation was broadened using the Gaussian function of $\Gamma = 1.0$ eV for comparison with the experimental spectrum. This method has been applied to a large number of ELNES and XANES calculations of ceramics [12, 16, 28–33], dopants [7, 8], defects [34, 35], interfaces [26, 36], solid solutions [37–39], and high-T_c superconductors [6, 40], with great success.

In order to extract the electronic structure information from the calculated spectra, the overlap population (OP) diagram has been computed. When atomic orbitals are used as basis functions, as in the OLCAO method, features that appear in theoretical spectra can be analyzed in terms of interactions among atomic orbitals in a straightforward manner. In the Mulliken scheme [41], the OP between orbitals i and j in the nth band is defined by

$$q^n_{i,\gamma,j,\delta} = \int A^{n*}_{i,\gamma}(k) \cdot A^n_{j,\delta}(k) \cdot S_{i,\gamma,j,\delta}(k) dk \quad (4)$$

where the overlap integral at k, $S_{i,\gamma,j,\delta}(k)$, is given by

$$S_{i,\gamma,j,\delta}(k) = \int b^*_{i,\gamma}(k, r) \cdot b_{j,\delta}(k, r) dr. \quad (5)$$

Here, the orbitals i and j belong to atoms a and b, respectively. A bond overlap population of a pair of atoms (a and b), $Q_{i,\gamma,j,\delta}$, is given by the summation of $q^n_{i,\gamma,j,\delta}$ over the occupied bands. In order to construct the OP

diagram, each of the overlap populations in the nth band is broadened with Gaussian functions of FWHM = 1.0 eV. When the band is occupied, positive and negative values of overlap population correspond to bonding and anti-bonding interactions, respectively. The same notation will be hereafter used for unoccupied bands.

2.2. Experimental procedure

Some of the experimental spectra were also obtained in this study. Mg $L_{2,3}$ and O K ELNES were observed by an FEI Tecnai F20 G2 UT transmission electron microscope operated at 200 kV. The microscope is equipped with an electron energy loss spectrometer (Tridiem Gatan imaging filter). The Mg $L_{2,3}$ edge was observed by using a double-focusing Wien filter acting as a monochromator below the field-emission gun. The energy resolution, namely the full width at half maximum of the zero-loss peak, for the Mg $L_{2,3}$ edge, was 0.3 eV. The Al $L_{2,3}$ and N K edges of AlN and the O K edge of ZnO were recorded using a transmission electron microscope with a field-emission gun (CM200FEG, FEI) with a CCD camera (GIF, Gatan) as a spectrum detector. The aperture size for the entrance of the spectrometer was 0.6 mm for the Al $L_{2,3}$ edge and 2.0 mm for both N K and O K edges. The energy calibration was made using the position of zero-loss peaks which were recorded before and after each measurement. Mg K, Al K, and Zn L_3 XANES was obtained at BL-1A and 7A of the soft x-ray beam line of UVSOR at the Institute for Molecular Science, Okazaki, Japan. The spectrum was collected in the total electron yield mode at room temperature using a beryl, $3(BeO)(Al_2O_3)6(SiO_2)$, two-crystal monochromator. The photon energy was calibrated at the Al K edge (1568 eV) from the beryl crystal. Zn K XANES was observed at BL01B1 in SPring-8, Nishi-Harima, Japan. In order to measure with high energy resolution, Si(311) double crystals were employed as monochromators. Fluorescence x-ray from the sample was detected using 19 sets of Ge solid state detectors.

3. Results and discussion

3.1. Overlap population diagrams for ELNES and XANES of MgO

Figures 1, 2, and 3 show the OP diagrams for Mg K, Mg $L_{2,3}$, and O K edges, respectively. Peaks in the experimental spectrum are named A_K to F_K, where the subscript 'K' denotes the peak in the Mg K edge. In the same manner, the subscripts 'L' and 'O' were used to show that the peaks are in the Mg $L_{2,3}$ edge and O K edge, respectively. The excited atom is distinguished using an asterisk. The calculations were performed with 128-atom supercells. Since the electric dipole selection rule allows only the transition from the Mg 1s to the unoccupied p orbitals, the OP diagrams with Mg* p are shown in figure 1 to interpret the Mg K edge. As can be learned from the figure, peaks A_K and D_K are determined by the bonding and anti-bonding interactions of Mg* p–Mg s. The peaks B_K and E_K can be mainly ascribed to the bonding and anti-bonding interactions of Mg* p–Mg p. The contribution of Mg* p–Mg d
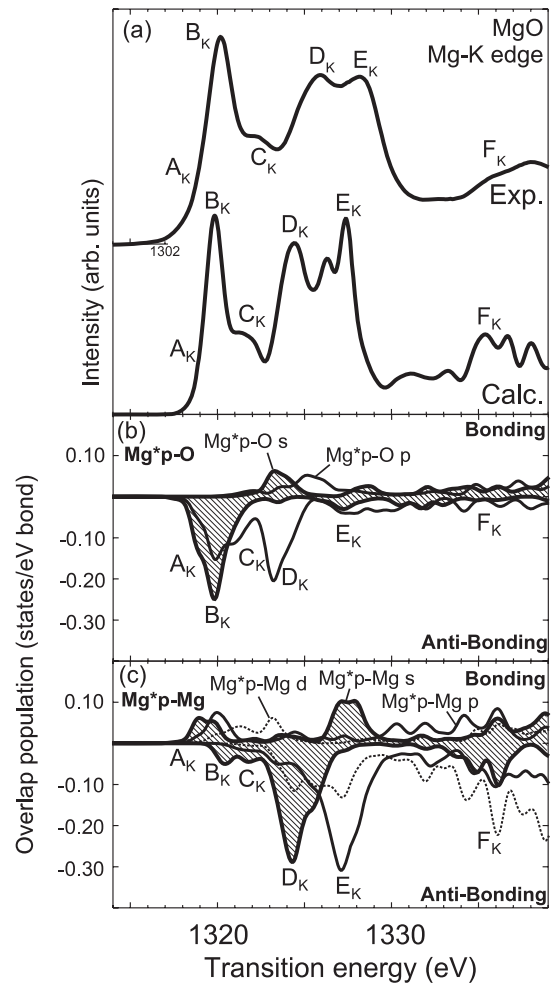

Figure 1. (a) The experimental and calculated Mg K edge and (b) the overlap population (OP) diagrams for Mg* p–O and (c) Mg* p–Mg bonds. The asterisk represents the Mg which has the core hole in the 1s core orbital.

interactions increases from the higher energy side of peak E_K, and peak F_K is mainly caused by the Mg* p–Mg d anti-bonding interaction.

For the Mg $L_{2,3}$ edge, both OP diagrams with Mg* s and Mg* d are displayed in figure 2. It is found that peaks A_L and B_L mainly originates from the Mg* s orbitals, whereas the contribution of Mg* d increases from peak C_L. Although both Mg* s and Mg* d orbitals make the bonding and anti-bonding interactions at the other peaks, the contribution of the Mg* s orbital is absent from peak E_L. Peak E_L mainly originates from the Mg* d–Mg d anti-bonding interaction. As can be seen from the OP diagrams, both peaks A_L and B_L have similar origins. The Mg* s–Mg s bonding and the Mg* s–Mg d anti-bonding are respectively weaker and stronger at peak B_L. On the other hand, the OP diagrams revealed that the presence of Mg* d–Mg d anti-bondings contributes to the splitting at peak F_L.

Figure 3 shows the experimental and calculated O K ELNES and the OP diagrams. As described above, the unoccupied bands are characterized by the Mg–Mg interactions. Therefore, not only the OP diagram for O*p–Mg$_1$ but also that between the surrounding Mg, namely Mg$_1$–Mg$_2$,
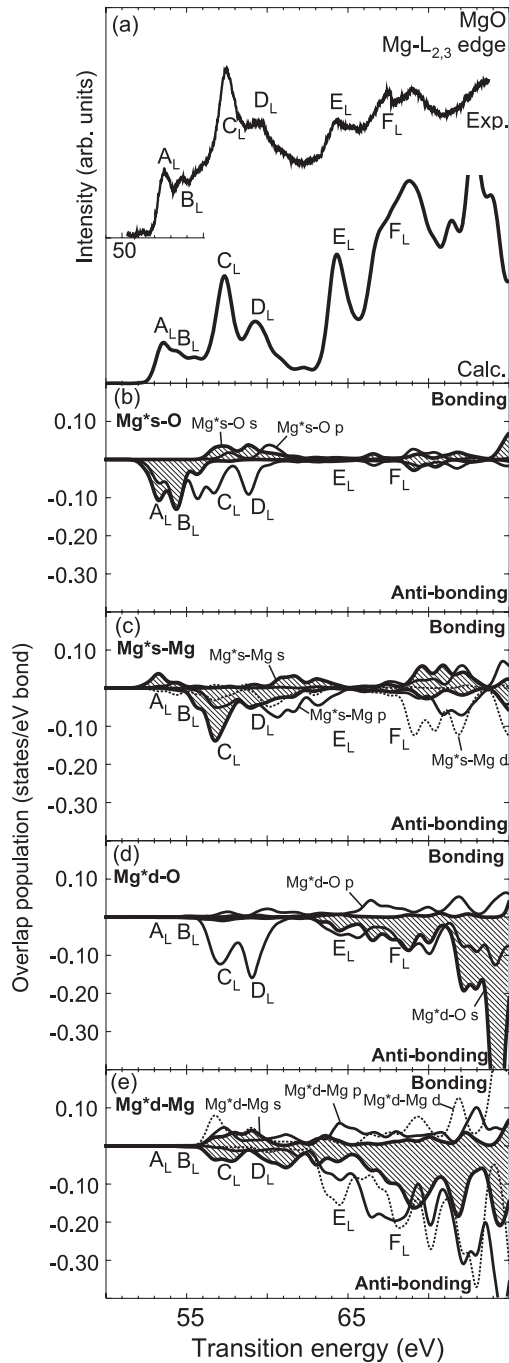
Figure 2. (a) The experimental and calculated Mg $L_{2,3}$ edge and (b) the overlap population (OP) diagrams for Mg* s–O, (c) Mg* s–Mg, (d) Mg* d–O, and (e) Mg* d–Mg. The asterisk represents the Mg which has the core hole in the 2p core orbital.

Figure 3. (a) The experimental and calculated O K edge and the overlap population (OP) diagrams for (b) O*p–Mg$_1$ and (c)–(e) Mg$_1$–Mg$_2$. The asterisk represents the O which has the core hole in the 1s core orbital.

are also displayed. The subscripts '1' and '2' for Mg represent the first and second nearest neighbor Mg to the excited oxygen, respectively. Regarding the O*–Mg$_1$ interactions, the anti-bonding interactions with the Mg$_1$ s orbital mainly contribute to peaks A_O, B_O, and C_O, whereas peak D_O originates from the strong anti-bonding interaction with Mg$_1$ p orbitals. The O*p–Mg$_1$d anti-bonding interactions mainly contribute to the other small peaks located at higher energy than peak E_O, although it also plays a role in peaks B_O and C_O.
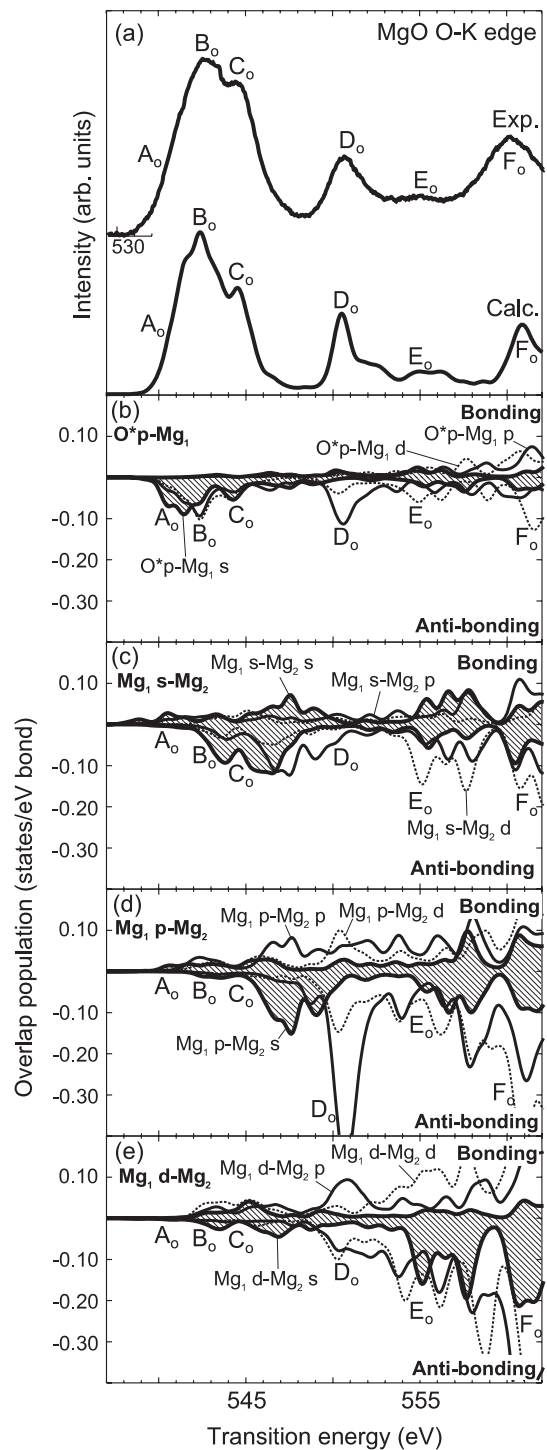
It is interesting to find the analogy between O K edge spectrum and spectra at the other Mg edges with respect to the Mg–Mg interactions. It is clearly found that the strong Mg$_1$p–Mg$_2$p anti-bonding interaction at peak D_O in the O K edge corresponds to that at peak E_K in the Mg K edge. In the same manner, the bonding interactions for Mg$_1$s–Mg$_2$s at
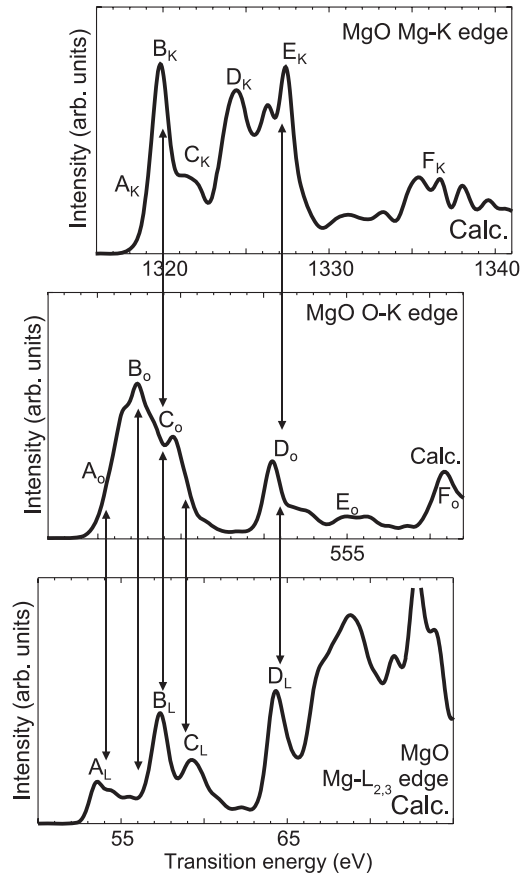
4

Figure 4. Three calculated spectra were aligned with the common features in the overlap population (OP) diagrams in figures 1–3.

peaks A_O and B_O and the anti-bonding Mg_1s–Mg_2s at peak C_O are respectively similar to those at peaks A_L, B_L, and C_L in the Mg $L_{2,3}$ edge. Here, it should be mentioned that the electronic structures of these different core-hole states are not necessarily comparable because the effects of respective core holes on the electronic structure are not identical [25]. For instance, the anti-bonding interaction for Mg^* p–Mg p at peak E_K in the Mg K edge is weaker than that at peak D_O in the O K edge. However, the core-hole effects are not strong enough to change the orbital interactions completely. Using such information, different edges can be aligned with some common features as shown in figure 4. These results are found to be consistent with our previous conclusion, which was obtained using a cluster method [10]. Although unoccupied PDOSs are separately observed as different edges and appear at different energies in ELNES and XANES, they can be reunited by using figure 4.

3.2. Overlap population diagrams for ELNES and XANES of wurtzite compounds

The OP diagram was applied to the ELNES and XANES from AlN, GaN, InN, and ZnO. These compounds have wurtzite structure under ambient conditions and have similar unoccupied band structure, which is composed of s-, p-, and d-type bands from the conduction band minimum [42, 43]. All calculations were performed with 108-atom supercells.

Experimental and calculated spectra and corresponding OP diagrams were shown in figures 5–7. Similar to the previous section, subscripts 'K', 'L', 'O', and 'N' represent peaks in the cation K edge, cation $L_{2,3}$ edge, O K edge, and N K edge, respectively. Subscripts '1' and '2' were used to represent the first and second nearest neighbor atomic sites. In the case of wurtzite structure, the first nearest neighbor atoms form tetrahedral coordination with two kinds of bond length, one longer length bond and three shorter length bonds. They are distinguished by using subscripts '(1)' and '(2)', respectively.

Figure 5 shows cation K edges and corresponding OP diagrams. In the Al K edge of AlN (figure 5(a)), it is found that peak A_K is mainly composed of Al^*3p–$N_{(1),(2)}$ anti-bonding interactions. On the other hand, though Ga K and In K edges are different edges of the different compounds, their A_K peaks are commonly composed of cation* p–$N_{(1),(2)}$ anti-bonding interactions. Comparing the A_K/C_K intensity ratios of these three nitrides, it is found that the ratio decreases with a decrease of the cation* p–anion anti-bonding interaction (figures 5(a)–(c)). The analogy of the peak assignments is also found in other peaks. Strong cation*–cation and cation*–$N_{(2)}$ anti-bonding interactions were commonly found in peak C_K, and peaks B_K and D_K are mainly composed of strong cation*–cation and cation*–$N_{(1)}$ anti-bonding interactions. Similar peak assignments are also found in the Zn K edge of ZnO (figure 5(d)). Peak A_K is composed of Zn^*–$O_{(1),(2)}$ anti-bonding interactions; Zn^*–$O_{(2)}$ anti-bonding interactions and Zn^*–$O_{(1)}$ anti-bonding interactions are respectively more significant at peak C_K and peaks B_K and D_K, and strong Zn^*–Zn interactions appear at peaks C_K and D_K. These assignments for the Zn K edge of ZnO are the same as those for the cation K edges of the nitrides (figures 5(a)–(d)).

Cation $L_{2,3}$ edges and OP diagrams of these wurtzite compounds are shown in figure 6. Similar to the K edges in figure 5, resembling assignments are found in all compounds. For instance, peaks A_L of all compounds are commonly composed of cation* s–anion$_{(1),(2)}$ anti-bonding interactions and cation* d–anion$_{(1),(2)}$ bonding interactions; the contributions of cation* s, d–anion$_{(1)}$ and cation* d–cation anti-bonding interactions are more significant at peaks B_L, and strong cation*–cation anti-bonding interactions appear around peaks D_L (figures 6(a)–(d)).

There is an interesting comparison between the OP diagrams for the Mg $L_{2,3}$ edge of MgO in figure 2 and those for the cation $L_{2,3}$ edge of the wurtzite compounds in figure 6. The characteristic difference can be found at peaks A_L and B_L. It is found that peaks A_L and B_L of the wurtzite compounds are composed of both cation* s and cation* d orbitals (figure 6), whereas Mg^* d orbitals do not contribute to peaks A_L and B_L in MgO (figure 2). This discrepancy is caused by the different local coordination in the crystals. Atoms in MgO, rock salt structure, form octahedral coordination with O_h symmetry, whereas atoms in the wurtzite structure have tetragonal coordination. When an isolated atom in these crystals is assumed, p orbitals cannot be hybridized with d orbitals in the O_h symmetry, whereas the p–d hybridization is allowed in the wurtzite structure [42, 43, 46]. In the crystals, cations and anions are bonded with each other and
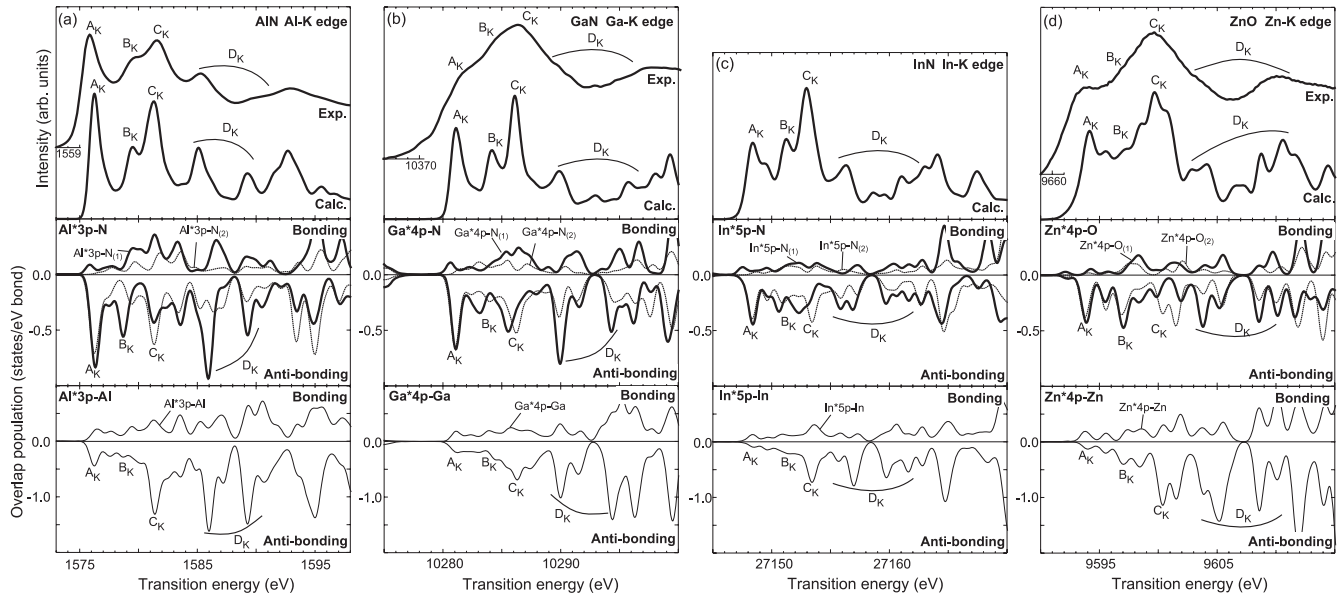
Figure 5. Experimental and calculated cation K edges and corresponding overlap population (OP) diagrams for (a) AlN, (b) GaN, (c) InN, and (d) ZnO. The experimental Ga K edge was obtained from [44]. The asterisk represents the atom which has the core hole at the 1s core orbital.
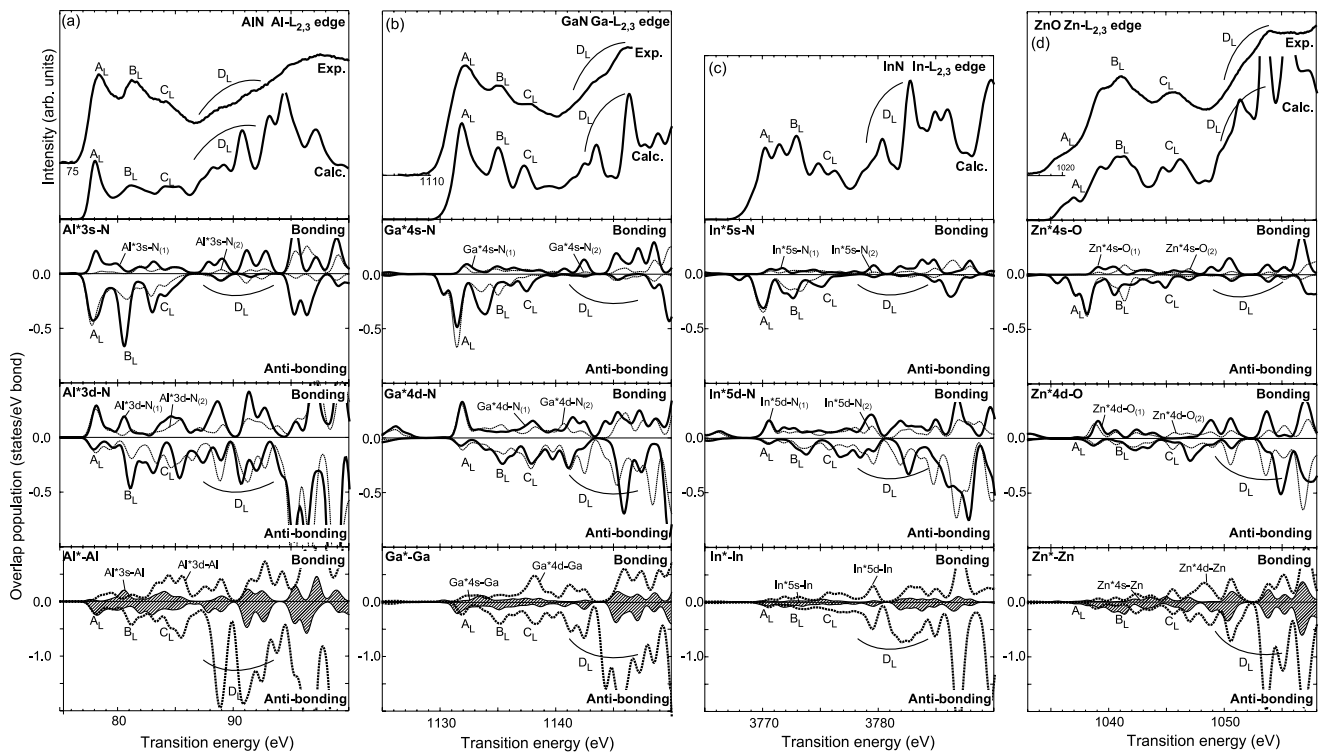

Figure 6. Experimental and calculated cation $L_{2,3}$ edges and corresponding overlap population (OP) diagrams for (a) AlN, (b) GaN, (c) InN, and (d) ZnO. The experimental Ga $L_{2,3}$ edge was obtained from [44]. The asterisk represents the atom which has the core hole in the 2p core orbital.

these orbitals are broadened. However, the degree of the band dispersion of the d orbital is expected to be broader in wurtzite structure than that in rock salt structure due to the presence of the p–d hybridization. The broader d orbitals can therefore contribute to the peaks on the lower energy side in the wurtzite compounds. This difference is important when the different edges are aligned with the same features in the OP diagrams, which is discussed later.

In the anion K edges, AlN has an intense peak A_N, whereas the peak A_N intensity decreases in GaN and InN (figures 7(a)–(c)). A similar decrement of peak A was found in cation K edges of these nitrides (figures 5(a)–(c)). This spectral difference is also ascribed to a decrease of N^*–cation anti-bonding interactions (figures 7(a)–(c)). On the other hand, the anion*–cation anti-bonding interactions at peak B_N are more
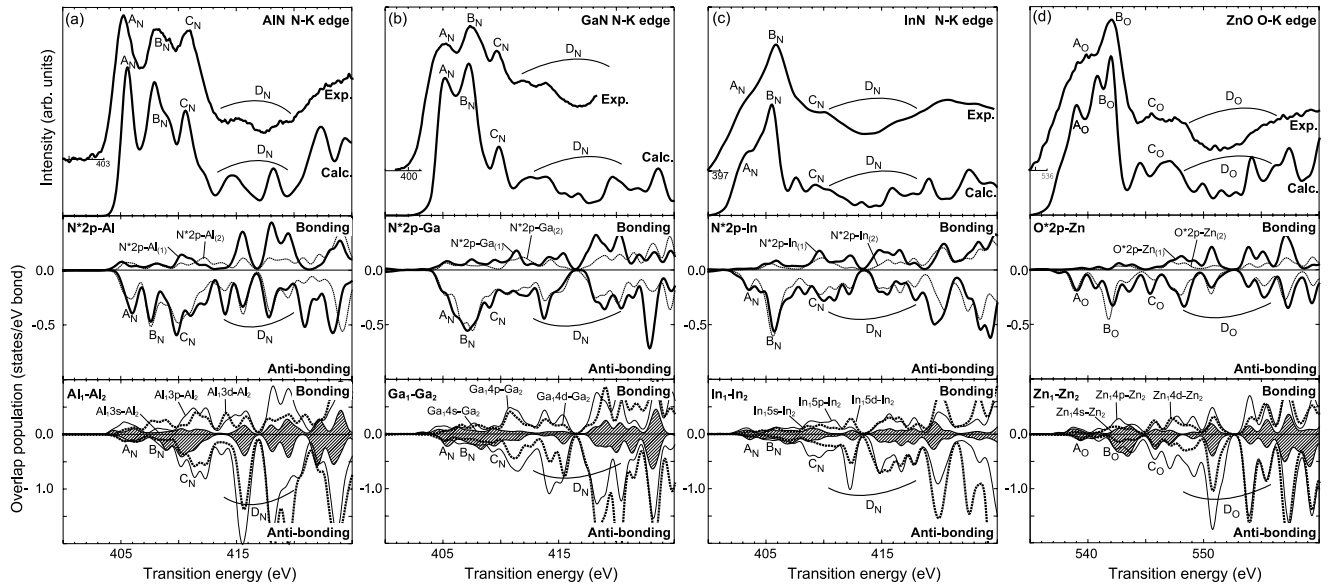
Figure 7. Experimental and calculated anion K edges and corresponding overlap population (OP) diagrams for (a) AlN, (b) GaN, (c) InN, and (d) ZnO. Experimental N K edges of GaN and InN were obtained from [44] and [45], respectively. The asterisk represents the atom which has the core hole at the 1s core orbital.
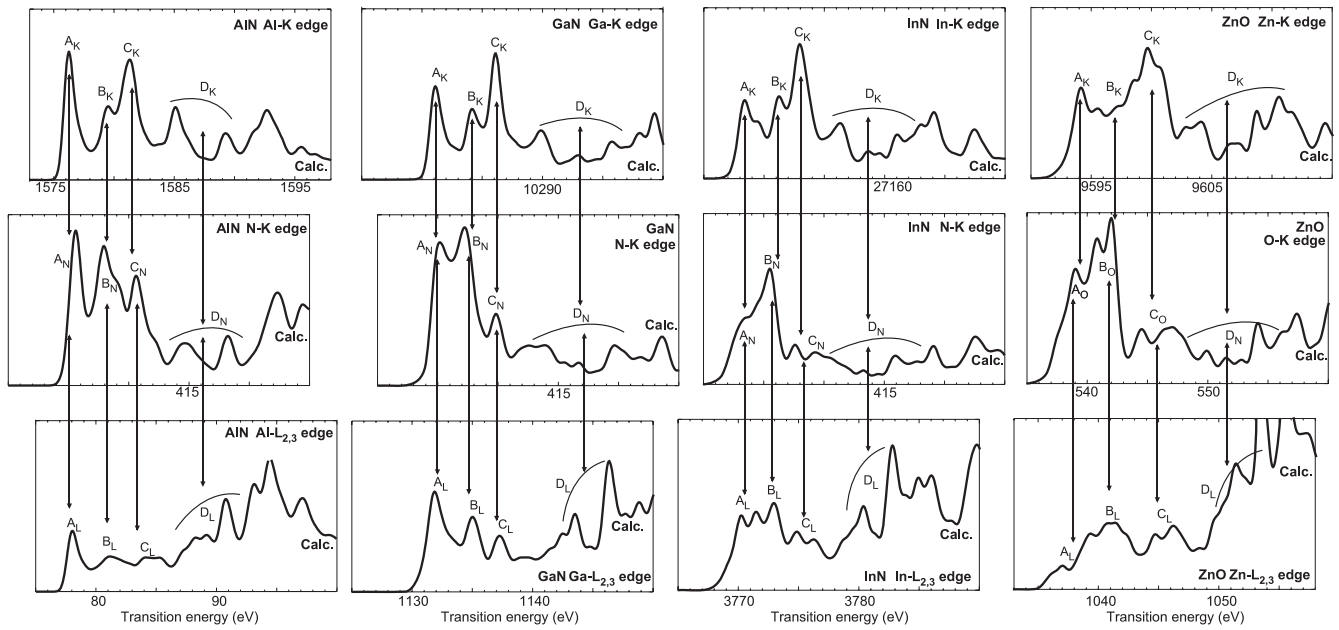

Figure 8. Calculated spectra were aligned with the common features in the overlap population (OP) diagrams in figures 5–7.

significant in GaN and InN, which contributes to the intense B_N peaks in these nitrides. The contribution of cation$_1$–cation$_2$ interactions increases at the higher energy peaks, and strong cation$_1$ p,d–cation$_2$ interactions are present at D_N peaks of all compounds. It is found that these peak assignments are applicable to the O K edge of ZnO (figure 7(d)). Namely, peaks A_O and B_O are composed of O*–Zn anti-bonding interactions and the Zn_1–Zn_2 interactions become dominant at the higher energy peaks C_O and D_O.

By comparing with those OP diagrams in figures 5, 6, and 7, it is found that the cation*–cation interactions at peaks D_K, D_L, and $D_{N,O}$ are very similar to each other. In addition, the cation–anion anti-bonding interactions commonly

contribute to the characteristic triple peak features, $A_{K,L,N,O}$, $B_{K,L,N,O}$, and $C_{K,L,N,O}$. By using these common features in the OP diagrams, different edges can be aligned as shown in figure 8. As compared with MgO in figure 4, it is found that the alignments are different from these wurtzite compounds. Peaks $A_{L,O}$ and $B_{L,O}$ do not correspond to any peak in the Mg K edge (figure 4), whereas all peaks in the cation K edges of the wurtzite compounds have the same assignments as the peaks in the cation $L_{2,3}$ edges and anion K edges (figure 8). As discussed above, this difference between the wurtzite compounds and MgO is caused by the local coordination of atoms in the crystals.
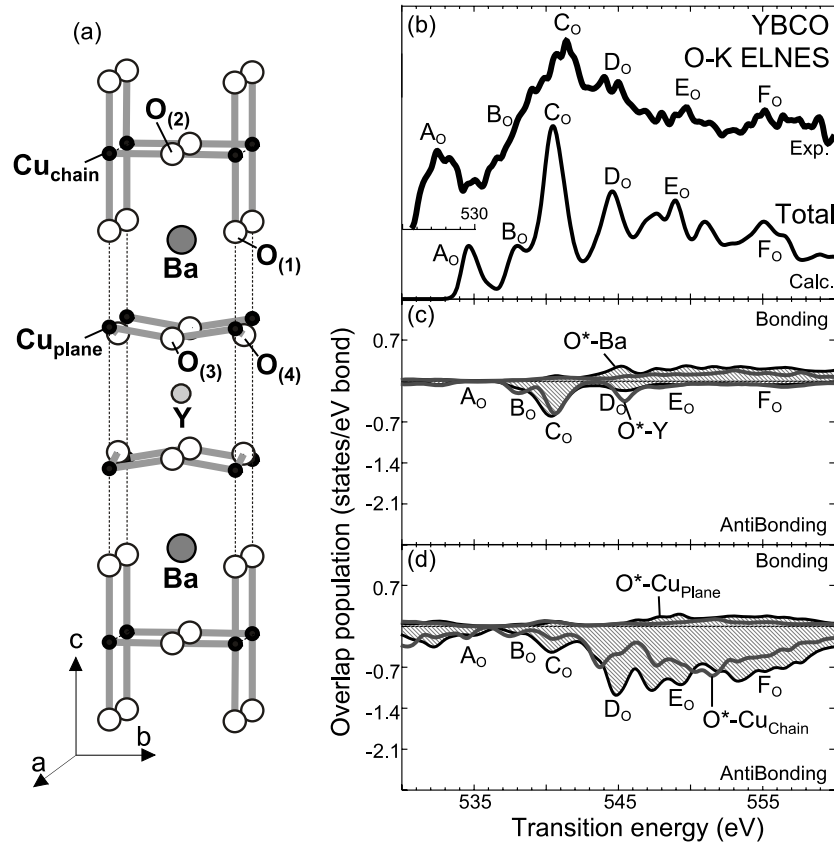
Figure 9. (a) Atomic structure of YBa$_2$Cu$_3$O$_{7-x}$ (YBCO) unit cell. (b) Calculated and experimental O K ELNES of YBCO, and (c), (d) the overlap population (OP) diagrams for O*–Ba/O*–Y and O*–Cu$_{Chain}$/O*–Cu$_{Plane}$ obtained by summing that of individual oxygens with a weight of the number of each atom in the unit cell. The asterisk represents the oxygen which has the core hole in the 1s core orbital.

From these results, it is concluded that similar peak assignments are possible even in different compounds when they have same crystal structure and conduction band structure.

3.3. Peak assignment of YBa$_2$Cu$_3$O$_{7-x}$ O K ELNES

Here, the OP diagram is applied to the O K ELNES of YBa$_2$Cu$_3$O$_{7-x}$ (YBCO). YBCO is one of the most prominent members of the high temperature superconductive oxides, and promising for commercial applications. The oxygen K XANES and ELNES have been widely used in YBCO studies because the intensity of their first peak is proportional to the hole concentration [47, 48]. On the other hand, in contrast to the first peak, the nature and subsequent assignment of the other peaks in the higher energy loss region have not been clarified so far. Since the wavefunctions giving rise to the higher energy peaks are more delocalized than the ones responsible for the appearance of the first peak, it is expected that they are more sensitive to changes in the local atomic and electronic structures. However, the interpretation of the spectrum using PDOS accompanies difficulties due to the complicated conduction band structures [40]. The OP diagram is effective for such complex systems.

As shown in figure 9(a), the unit cell of YBCO has several inequivalent O positions: two plane oxygens, O$_{(3)}$ and O$_{(4)}$, one chain oxygen, O$_{(2)}$, and the apical oxygen between the

chain and the plane, O$_{(1)}$ [49]. Therefore, the core hole was introduced at each site and the spectrum was calculated separately. In order to introduce the core hole accurately, 117 atom supercells were constructed by replicating the YBCO unit cell $3 \times 3 \times 1$ times. Figure 9(b) shows the experimental and calculated O K ELNES of YBCO. In order to compare with the experimental spectrum, the calculated spectra from four oxygens were summed with a weight considering the number of sites contained in the unit cell. The individual spectrum and OP diagram for each site have been shown elsewhere [6, 40]. The experimental spectrum was obtained with a 2 nm wide electron probe and thus the site dependence could not be detected [6]. The error in the transition energy is about 5.0 eV, which is less than 1% of the absolute transition energy. It can be seen that the total calculated spectrum reproduces well the experimental spectrum, except for the position of peak A. Peak A originates from the interactions between O 2p and partially occupied Cu d orbital [6, 40]. For the quantitative reproduction of peak A, effects of strong electron–electron correlations, such as the Mott–Hubbard term '$+U$', are necessarily included in the calculation [50].

Figures 9(c) and (d) show the total OP diagrams obtained by summing those of individual oxygen sites with a weight of the number of each site found in the unit cell. From the OP diagrams, the peaks in the YBCO O K ELNES are interpreted to be as follows. (1) The contributions of Y and
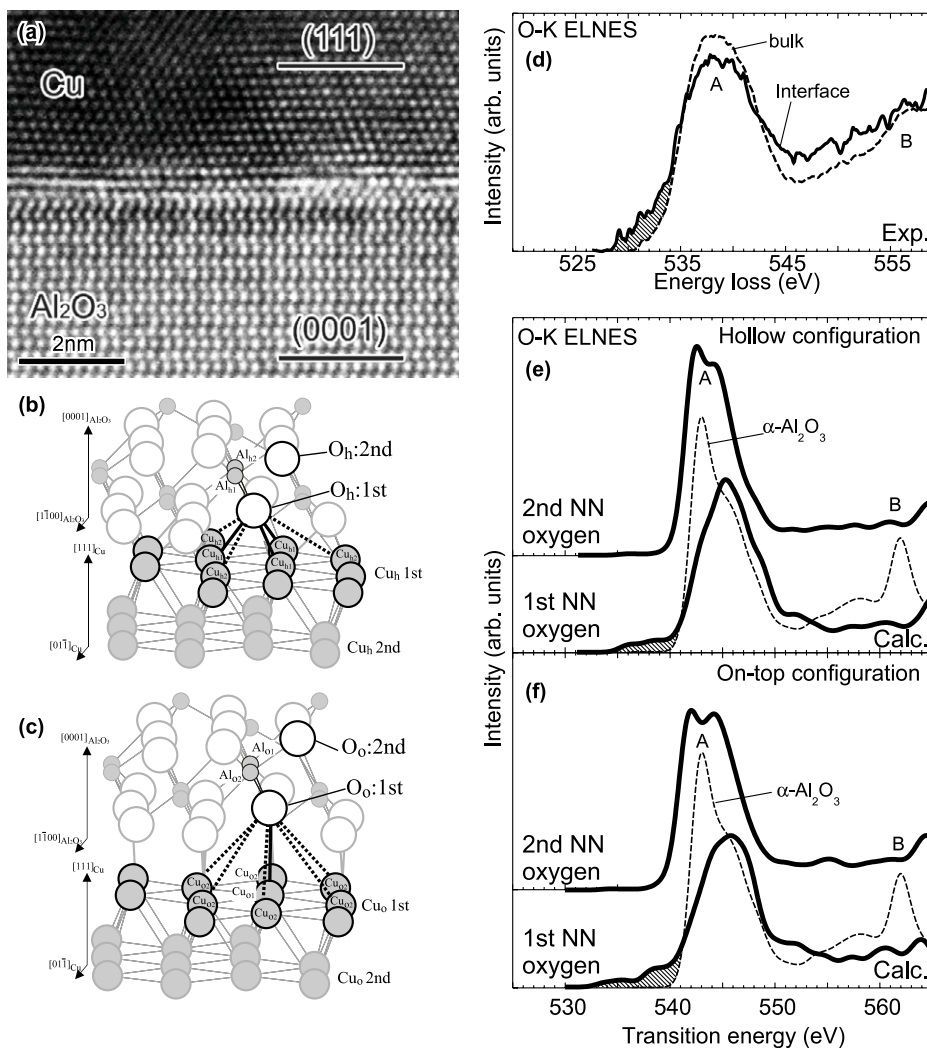
Figure 10. (a) HRTEM image of the Cu(111)/Al$_2$O$_3$(0001) interface [53, 54], (b), (c) atomic structures around the interface with hollow and on-top configurations, (d) experimental O K ELNES from the Al$_2$O$_3$ bulk and Cu/Al$_2$O$_3$ interface [53, 54], and (e), (f) calculated O K ELNES from the first and second nearest neighbor (NN) oxygens to the hollow and on-top interfaces. Calculated ELNES of Al$_2$O$_3$ are superimposed with dashed lines.

Ba are almost negligible at peak A. (2) Peaks B and C are composed of all O*–Cu, O*–Y, and O*–Ba interactions. (3) The largest O*–Cu interactions appear at peak D. (4) The peaks higher in energy than peak D are mainly caused by the O*–Cu anti-bonding interactions. Those assignments suggest that the first and fourth peaks and the second and third peaks can be sensitive to the atomic and electronic structure changes at the Cu and Y/Ba sites, respectively. The OP diagram is powerful to interpret ELNES and XANES from such compounds, which have complex atomic and electronic structures.

3.4. Relationships between ELNES and interface strength of Cu/Al$_2$O$_3$ interface

Here, the OP diagram was applied to the Cu/Al$_2$O$_3$ interface in order to find relationships among ELNES, chemical bonding, and physical properties. Cu/Al$_2$O$_3$ is known as a typical metal/ceramic hetero-interface and is studied with experimental and theoretical approaches [26, 51–55].

Figure 10(a) shows a typical HRTEM image of the Cu(111)/Al$_2$O$_3$(0001) interface [53, 54]. The interface has been known as an incoherent interface, and does not have misfit dislocations or specific periodicities of atomic arrangements. Due to the lack of periodicity, the interface is composed of many kinds of atomic configurations, such as on-top, bridge, and hollow. The interface strength of the hollow configuration (figure 10(b)) and on-top configuration (figure 10(c)) were theoretically investigated, and it was concluded that the hollow configuration is stronger than the on-top configuration [55, 56]. O K ELNES from the interface was also observed, and it was reported that a pre-peak feature in front of the main peak appears when the O K ELNES is observed from the interface (figure 10(d)) [52–54]. The OP diagram was applied to elucidate how the different atomic configurations of the interface affect chemical bondings, interface strength, and ELNES.

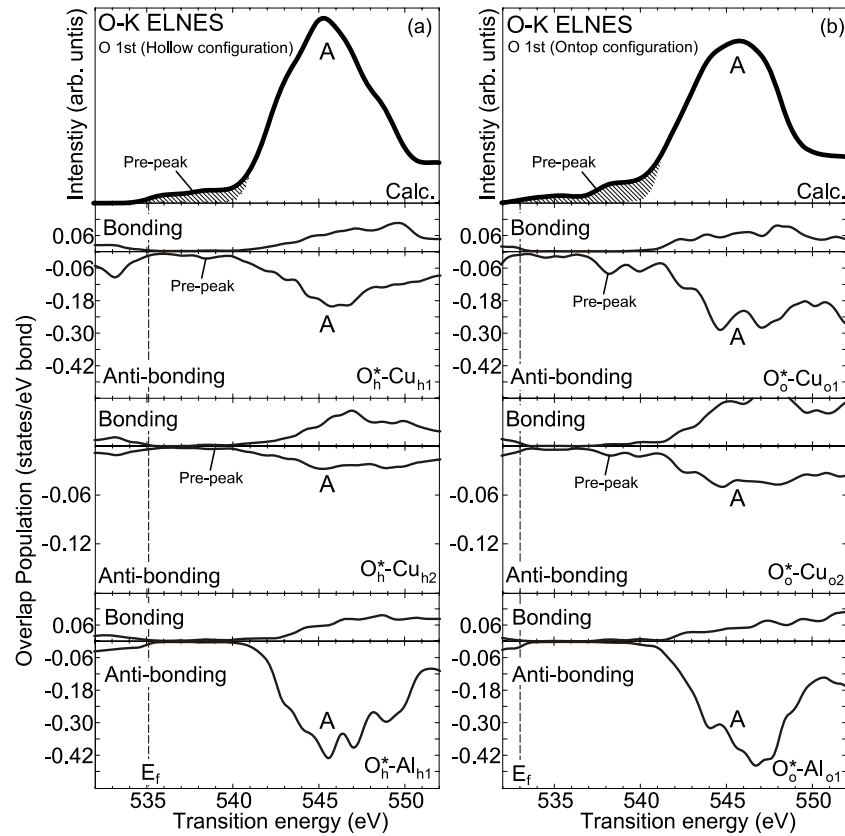Figures 10(d)–(f) show the experimental [53, 54] and calculated O K ELNES. The interface model was obtained

Figure 11. Calculated O K ELNES and corresponding overlap population (OP) diagrams for (a) the hollow configuration and (b) the on-top configuration. The asterisk represents the oxygen which has the core hole in the 1s core orbital. Thin dashed lines represent the position of the top of the valence band.

in a previous study by a first principles pseudopotential method [55]. An interfacial oxygen and the first and second nearest neighbor Cu and Al are called 'O', 'Cu$_1$', 'Cu$_2$', 'Al$_1$', and 'Al$_2$', respectively. The subscripts 'h' and 'o' are used when it is necessary to distinguish atoms in the hollow and on-top configurations. The calculated spectra from the first and second nearest neighbor oxygens to the interfaces were separately obtained by introducing the core hole at the respective oxygen. Although the onsets of the calculated spectra were shifted by +6 eV, it should be noted that the calculation error is less than 1.2% of the absolute transition energy. The calculated O K ELNES of α-Al$_2$O$_3$ is superimposed on that of the first nearest neighbor oxygen. As compared with α-Al$_2$O$_3$, it is found that peak A is broader and peaks A and B slightly shift to the higher energy side in both interface models. A characteristic feature for the interfacial oxygens can be found at the front of peak A, i.e. the pre-peak. This is shaded in the figure. By comparing the size of the shaded area, it was found that the pre-peak for the on-top configuration is 57% larger than that for the hollow configuration. At the second nearest neighbor oxygen sites, it is found that the pre-peak intensity remarkably decreases. This indicates that the pre-peak mainly originates from the interfacial O–Cu interactions.

In order to interpret the calculated spectra, the OP diagrams of the conduction bands in the final state were

computed. Figure 11 shows the OP diagrams of O*–Cu$_1$, O*–Cu$_2$, and O*–Al$_1$. In order to focus the pre-peak, the energy region between the pre-peak and peak A is magnified. It is found that peak A and the pre-peak mainly originate from the O*–Al and the O*–Cu anti-bonding interactions, respectively. Both bonding and anti-bonding interactions in the pre-peak area of the on-top configuration are 50–78% larger than that of the hollow configuration. Therefore, the larger pre-peak in the on-top configuration is ascribed to the larger O*–Cu interactions, including bonding and anti-bonding.

Regarding the relationship between the pre-peak and the interface strength, the integrated pre-peak intensity is larger in the on-top interface, whereas the on-top interface is weaker than the hollow interface. From the previous study, it was revealed that the weakness of the on-top configuration is caused by the larger anti-bonding interactions [26]. That is to say, the larger anti-bonding interactions in the on-top configuration cause the larger pre-peak in the O K ELNES and the weaker interface.

As demonstrated here, the relationships between the spectral features and the physical properties are not always direct or proportional. In the case of the Cu/Al$_2$O$_3$ interface, the integrated pre-peak intensity is inversely proportional to the interface strength. To find intersections between ELNES and physical properties, peak assignments and detailed investigations of the electronic structures are indispensable.

4. Summary

In this review, the overlap population (OP) diagram was systematically applied to ELNES and XANES. All peaks in the spectra were interpreted in terms of cation–anion and cation–cation interactions. Through the peak assignments, it was found that same features are found in the OP diagrams even in different edges and different compounds. PDOSs in the unoccupied bands are separately observed as different edges and appear at different energies in the ELNES and XANES. However, they can be aligned with common features in the OP diagrams. This alignment of ELNES and XANES corresponds to a reconstruction of the unoccupied electronic structures.

It has often been claimed that ELNES and XANES have a potential to provide information on atomic and electronic structures and chemical bondings. However, the relationships among spectral features, atomic and electronic structures, and physical properties are usually ambiguous, as shown in this review. Simple 'reproduction' is not enough to extract the atomic and electronic structure information from the ELNES and XANES. Peak assignments and interpretations are indispensable to fully utilize the spectra. I believe that this review has demonstrated that the OP diagram is very powerful to give assignments and interpret the ELNES and XANES and find connections among spectral features, atomic and electronic structures, and physical properties.

Acknowledgments

References

[1] Stöhr J 1992 *NEXAFS Spectroscopy* (Berlin: Springer)
[2] Egerton R F 1996 *Electron Energy-Loss Spectroscopy in the Electron Microcopy* (New York: Plenum)
[3] Tanaka I, Mizoguchi T and Yamamoto T 2005 *J. Am. Ceram. Soc.* **88** 2013
[4] Varela M, Findlay S D, Lupini A R, Christen H M, Borisevich A Y, Dellby N, Krivanek O R, Nellist P D, Oxley M P, Allen L J and Pennycook S J 2004 *Phys. Rev. Lett.* **92** 95502
[5] Kimoto K, Aasaka T, Nagai T, Saito M, Matsui Y and Ishizuka K 2007 *Nature* **450** 702
[6] Mizoguchi T, Varela M, Buban J P, Yamamoto T and Ikuhara Y 2008 *Phys. Rev. B* **77** 024504
[7] Tanaka I, Mizoguchi T, Matsui M, Yoshioka S, Adachi H, Yamamoto T, Okajima T, Umesaki M, Chig W Y, Inoue Y, Mizuno M, Araki H and Shirai Y 2003 *Nat. Mater.* **2** 541
[8] Mizoguchi T, Sakurai M, Nakamura A, Matsunaga K, Tanaka I, Yamamoto T and Ikuhara Y 2004 *Phys. Rev. B* **70** 153101
[9] Tanaka I and Adachi H 1996 *Phys. Rev. B* **54** 4604
[10] Mizoguchi T, Tanaka I, Yoshiya M, Oba F, Ogasawara K and Adachi H 2000 *Phys. Rev. B* **61** 2180
[11] Lie K, Høier R and Brydson R 2000 *Phys. Rev. B* **61** 1786
[12] Mo S D and Ching W Y 2000 *Phys. Rev. B* **62** 7901
[13] Elsässer C and Köstlmeier S 2001 *Ultramicroscopy* **86** 325
[14] Moreno M S, Jorissen K and Rehr J J 2007 *Micron* **38** 1
[15] Hébert C 2007 *Micron* **38** 12
[16] Mizoguchi T, Tanaka I, Yoshioka S, Kunisu M, Yamamoto T and Ching W Y 2004 *Phys. Rev. B* **70** 45103
[17] Suga T, Kameyama S, Yoshioka S, Yamamoto T, Tanaka I and Mizoguchi T 2005 *Appl. Phys. Lett.* **86** 163113
[18] Yamamoto T, Mizoguchi T and Tanaka I 2005 *Phys. Rev. B* **71** 245113
[19] Ching W Y and Rulis P 2006 *Phys. Rev. B* **73** 045202
[20] Gao S P, Pickard C J, Payne M C, Zhu J and Yuan J 2008 *Phys. Rev. B* **77** 115122
[21] Radtke G, Saul A, Dabkowska H A, Gaulin B D and Botton G A 2008 *Phys. Rev. B* **77** 125130
[22] Ching W Y, Ouyang L Z, Rulis P and Yao H Z 2008 *Phys. Rev. B* **78** 014106
[23] Mizoguchi T, Tanaka I, Gao S P and Pickard C J 2008 submitted
[24] Hoffmann R 1987 *Angew. Chem. Int. Edn Engl.* **26** 846
[25] Mizoguchi T, Tatsumi K and Tanaka I 2006 *Ultramicroscopy* **106** 1120
[26] Mizoguchi T, Sasaki T, Matsunaga K, Tanaka S, Yamamoto T, Kohyama M and Ikuhara Y 2006 *Phys. Rev. B* **74** 235408
[27] Ching W Y 1990 *J. Am. Ceram. Soc.* **73** 3135
[28] Xu Y N, Chen Y, Mo S D and Ching W Y 2002 *Phys. Rev. B* **65** 235105
[29] Kimoto K, Ishizuka K, Mizoguchi T, Tanaka I and Matsui Y 2003 *J. Electron Microsc.* **52** 299
[30] Kimoto K, Matsui Y, Nabatame T, Yasuda T, Mizoguchi T, Tanaka I and Toriumi A 2003 *Appl. Phys. Lett.* **83** 4306
[31] Ching W Y and Rulis P 2008 *Phys. Rev. B* **77** 035125
[32] Aryal S, Rulis P and Ching W Y 2008 *Am. Mineral* **93** 114
[33] Ching W Y and Rulis P 2008 *Phys. Rev. B* **77** 125116
[34] Sato Y, Mizoguchi T, Oba F, Yodogawa M, Yamamoto T and Ikuhara Y 2004 *Appl. Phys. Lett.* **84** 5311
[35] Mizoguchi T, Sato Y, Buban J P, Matsunaga K, Yamamoto T and Ikuhara Y 2005 *Appl. Phys. Lett.* **87** 241920
[36] Rulis P, Ching W Y and Kohyama M 2004 *Act. Mater.* **52** 3009
[37] Tatsumi K, Mizoguchi T, Yoshioka S, Yamamoto T, Suga T, Sekine T and Tanaka I 2005 *Phys. Rev. B* **71** 033202
[38] Mizoguchi T, Seko A, Yoshiya M, Yoshida H, Yoshida T, Ching W Y and Tanaka I 2007 *Phys. Rev. B* **76** 195125
[39] Kunisu M, Tanaka I, Yamamoto T, Suga T and Mizoguchi T 2004 *J. Phys.: Condens. Matter* **16** 3801
[40] Mizoguchi T, Buban J P, Matsunaga K, Yamamoto T and Ikuhara Y 2006 *Ultramicroscopy* **106** 92
[41] Mulliken R S 1955 *J. Am. Chem. Soc.* **23** 1823
[42] Mizoguchi T, Tanaka I, Kunisu M, Yoshiya M, Adachi H and Ching W Y 2003 *Micron* **34** 249
[43] Mizoguchi T, Yamamoto T, Suga T, Kunisu M, Tanaka I and Adachi H 2004 *Mater. Trans.* **45** 2023

[44] Chiou J W, Jan J C, Tsai H M, Pong W F, Tsai M H, Hong I H,
Klauser R, Lee J F, Hsu C W, Lin H M, Chen C C,
Shen C H, Chen L C and Chen K H 2003 *Appl. Phys. Lett.*
82 3949

[45] Mkhoyan K A, Silcox J, Alldredge E S, Ashcroft N W, Lu H,
Schaff W J and Eastman L F 2003 *Appl. Phys. Lett.* **82** 1407

[46] Mizoguchi T, Yoshiya M, Li J, Oba F, Tanaka I and
Adachi H 2001 *Ultramicroscopy* **86** 363

[47] Yarmoff J A, Clarke D R, Drube W, Karlsson U O,
Taleb-Ibrahimi A and Himpsel F J 1987 *Phys. Rev. B*
36 3967

[48] Nücker N, Fink J, Fuggle J C, Durham P J and
Timmerman W M 1988 *Phys. Rev. B* **37** 5158

[49] Beno M A, Soderholm L, Capone D W, Hinks D G,
Jorgensen J J, Grace J D and Schuller I K 1987 *Appl. Phys.
Lett.* **51** 57

[50] Novák P, Boucher F, Gressier P, Blaha P and Schwarz K 2001
Phys. Rev. B **63** 235114

[51] Dehm G, Rühle M, Ding G and Raj R 1995 *Phil. Mag. B*
71 1111

[52] Scheu C, Dehm G, Rühle M and Brydson R 1998 *Phil. Mag. A*
78 439

[53] Sasaki T, Matsunaga K, Ohta H, Hosono H, Yamamoto T and
Ikuhara I 2003 *Sci. Technol. Adv. Mater.,* **4** 575

[54] Sasaki T, Mizoguchi T, Matsunaga K, Tanaka S, Yamamoto T,
Kohyama M and Ikuhara Y 2005 *Appl. Surf. Sci.*
241 87

[55] Tanaka S, Yang R, Kohyama M, Sasaki T, Matsunaga K and
Ikuhara Y 2004 *Mater. Trans.* **45,** 1973

[56] Hashibon A, Elsässer C and Rühle M 2005 *Act. Mater.*
53 5323